Synergistic Effect of Titanate-Anatase Heterostructure and Hydrogenation-Induced Surface Disorder on Photocatalytic Water Splitting

Jinmeng Cai,[†] Yingming Zhu,[†] Dongsheng Liu,[†] Ming Meng,*[,†] Zhenpeng Hu,*[,‡] and Zheng Jiang[§]

[†]Collaborative Innovation Center of Chemical Science & Engineering (Tianjin), Tianjin Key Laboratory of Applied Catalysis Science & Engineering, School of Chemical Engineering & Technology, Tianjin University, Tianjin 30072, P. R. China

[‡]School of Physics, Nankai University, Tianjin 300071, P. R. China

[§]Shanghai Synchrotron Radiation Facility, Shanghai Institute of Applied Physics, Chinese Academy of Sciences, Shanghai 201204, P. R. China

S *Supporting Information*

ABSTRACT: Black TiO$_2$ obtained by hydrogenation has attracted enormous attention due to its unusual photocatalytic activity. In this contribution, a novel photocatalyst containing both a titanate–anatase heterostructure and a surface disordered shell was in situ synthesized by using a one-step hydrogenation treatment of titanate nanowires at ambient pressure, which exhibited remarkably improved photocatalytic activity for water splitting under simulated solar light. The as-hydrogenated catalyst with a heterostructure and a surface disordered shell displayed a high hydrogen production rate of 216.5 μmol·h^{-1}, which is ~20 times higher than the Pt-loaded titanate nanowires lacking of such unique structure. The in situ-generated heterostructure and hydrogenation-induced surface disorder can efficiently promote the separation and transfer of photoexcited electron–hole pairs, inhibiting the fast recombination of the generated charge carriers. A

general synergistic effect of the heterostructure and the surface disordered shell on photocatalytic water splitting is revealed for the first time in this work, and the as-proposed photocatalyst design and preparation strategy could be widely extended to other composite photocatalytic systems used for solar energy conversion.

KEYWORDS: *heterostructure, hydrogenation, surface disorder, photocatalytic, water splitting*
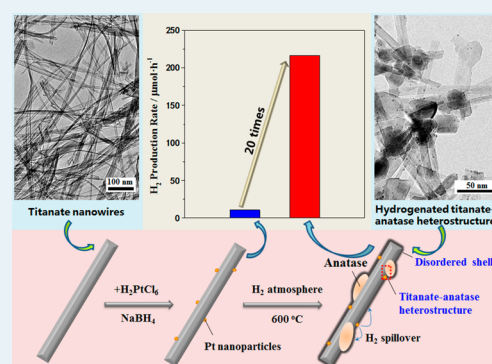
1. INTRODUCTION

Solar energy utilization is a promising and sustainable strategy to ultimately solve the problems of fossil fuel shortage and the related environmental pollution. Among various conversion systems, semiconductor-based photocatalysts for hydrogen evolution from water has been considered as a promising and environmentally friendly route for the efficient utilization of solar energy.[1−5] However, many investigated photocatalysts show low activity for water splitting due to the rapid recombination of photogenerated electrons and holes (e$^-$−h$^+$).[6] It is reported that nearly 90% of e$^-$−h$^+$ pairs can quickly recombine within 10 ns, which remarkably limits the performance of photocatalysts.[7] So, it is highly necessary to increase the separation and migration efficiency of charge carries during photocatalytic reactions.

Although metal[8] or nonmetal[9−12] doping can improve the activity of photocatalysts to some extent, the introduced dopants may also act as charge recombination centers, restricting the further increase of photocatalytic efficiency. Recently, black TiO$_2$ obtained by hydrogenation treatments has attracted enormous attention due to its greatly increased charge transfer capability and improved photocatalytic activity.[13−22]

Chen et al. first demonstrated that the black TiO$_2$ nanoparticles could be prepared in high-pressure hydrogen atmosphere at 200 °C for 5 days.[16] The obtained black TiO$_2$ with a thin amorphous layer encapsulating the anatase core exhibited remarkably enhanced hydrogen production rate due to the obviously narrowed optical band gap and surface disorder. To overcome the shortcomings of the rigorous hydrogenation conditions such as high pressure, excessive treating time, and potential explosion risks, Zhu et al. introduced the concept of hydrogen spillover to hydrogenation of TiO$_2$ by adding a small amount of Pt to it; with the assistance of hydrogen spillover effect of Pt, deeply hydrogenated TiO$_2$ was successfully obtained at normal atmospheric pressure; the as-formed surface disordered shell greatly enhanced the migration and separation of e$^-$−h$^+$ pairs and thus significantly increasing the photocatalytic performance of TiO$_2$ for water splitting.[20]

In addition, fabrication of heterostructure between different semiconductors is another efficient way to promote the separation and migration of e$^-$−h$^+$ pairs.[23−28] It is reported

that the 1D-nanostructured titanate nanowires are favorable to the transfer of electrons, which can effectively prevent the rapid recombination of e^-–h^+ pairs.[29] Anatase TiO_2 is a widely investigated metal oxide for its good photocatalytic property and stability. Both the crystal lattices of titanate and anatase consist of TiO_6 octahedra sheets by sharing four edges,[30,31] thus the in situ formation of heterostructure between anatase and titanate nanowires is possible due to their similar structure features. Across the titanate–anatase heterojunction, more efficient charge separation and transfer as well as higher photocatalytic performance can be achieved.

On the basis of the above analysis, we designed and in situ synthesized a titanate–anatase composite photocatalyst simultaneously possessing a nanoheterostructure and a homogeneous surface disordered shell via a one-step hydrogenation treatment at ambient pressure (Figure 1). The hydrogen
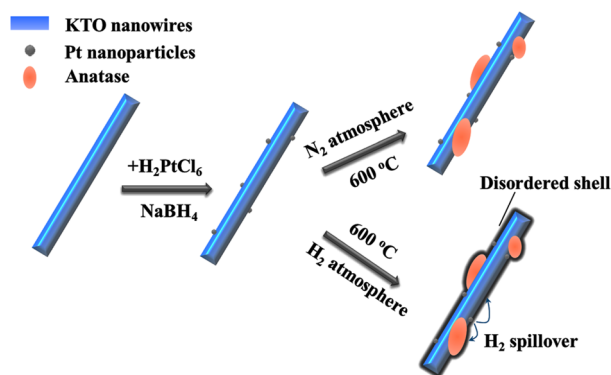

Figure 1. Schematic illustration for the preparation of the titanate–anatase heterostructure with surface disordered shell.

spillover from the preloaded Pt nanoparticles to the titanate–anatase heterostructure greatly enhanced the formation of the homogeneous surface disordered shell. The as-prepared catalyst exhibited a high photocatalytic hydrogen production rate of 216.5 μmol·h^{-1}, ~20 times larger than that of the catalyst without the heterostructure and surface disordered shell. The correlation between the catalytic performance and the catalyst structures including bulk, surface, and band structures is well established, and a general synergistic effect of the in situ-generated titanate–anatase heterostructure and the hydrogenated surface disordered shell on photocatalytic activity is proposed. Importantly, this is the first time to demonstrate that the photocatalytic performance can be remarkably improved by the synergistic effect of heterostructure and surface disordered shell. The photocatalyst design and synthesis strategy reported in this work would provide a facile yet effective route to develop other efficient solar-light-driven photocatalysts.

2. EXPERIMENTAL SECTION

2.1. Preparation of $K_2Ti_6O_{13}$ (KTO) Nanowires and Pt/KTO. In a typical procedure, 2 g of polyethylene glycol (PEG-800) was first dissolved in 28 mL of ethanol to obtain the solution A. Meanwhile, 0.68 g of tetrabutyl titanate (TBOT) was dissolved in 20 mL of ethanol to obtain solution B, which was subsequently added to solution A under vigorous stirring for 30 min to produce solution C. Then, 24 mL of KOH solution (2 M) with the volume ratio of 1:1 for deionized water to ethanol was added to the solution C. After continuous stirring for 30 min, the mixture was transferred into a 100 mL

Teflon-lined stainless steel autoclave, which was sealed and heated at 200 °C for 12 h. Afterward, the autoclave was cooled to room temperature naturally, and the product was collected by centrifuging the mixture; through washing three times with formic acid (0.1 M), deionized water, and absolute ethanol, the precursor was obtained, which was dried at 60 °C in vacuum for 12 h to produce the $K_2Ti_6O_{13}$ nanowires (denoted as KTO). The Pt/KTO with 1 wt % Pt loaded on KTO was synthesized by using the conventional wetness impregnation method. Typically, 2 g of KTO was first immersed into a certain amount of H_2PtCl_6·$6H_2O$ aqueous solution to acquire a slurry, which was subsequently dried at room temperature for 24 h; then the dried powder was dispersed into 400 mL deionized water and reduced by 440 mg of $NaBH_4$. By centrifugation, the catalyst precursor was obtained and washed with deionized water.

2.2. Preparation of Titanate–Anatase Heterostructure. The Pt/KTO were annealed in pure nitrogen atmosphere (30 mL/min) at 400, 600, or 800 °C for 5 h, respectively, the final samples are denoted as N-x, x = 400, 600, or 800. Hydrogen treatment was carried out in a tube furnace system. The Pt/KTO was further annealed in 10 vol % H_2/N_2 atmosphere (30 mL/min) at 600 °C for 5 h (denoted as H-600) to obtain the in situ-generated and hydrogenated titanate–anatase heterostructure.

2.3. Materials Characterization. The field emission scanning electron microscopy (FESEM) images of the samples were taken on a Hitachi S-4800 scanning electron microscope (SEM, 5 kV), equipped with a Thermo Scientific X-ray fluorescence analyzer for energy-dispersive X-ray spectroscopic (EDS) analysis. The images of transmission electron microscopy (TEM) and high-resolution transmission electron microscopy (HRTEM) as well as the EDS line scanning spectra were obtained by using a JEOL-JEM-2100F electron microscope operating at 200 kV. The specimens were prepared by dropping a droplet ethanol suspension on a copper grid coated with a 5 nm thickness of amorphous carbon film. The X-ray diffraction (XRD) patterns of the samples were recorded on a D/max 2500v/pc (Rigaku) diffraction instrument operating at 200 mA and 40 kV, using Cu Kα as the radiation source (λ = 0.15418 nm). The diffraction data were collected in the range of 2θ angle from 5 to 80° at a stepsize of 0.133° per second. The UV–vis diffuse reflectance spectra (UV–vis DRS) of the catalysts were recorded on a Lambda 750S UV–vis–NIR spectrometer (PerkinElmer) equipped with an integrating sphere. The UV–vis DRS spectra were recorded from the wavelength of 200 to 1500 nm against barium sulfate. The X-ray photoelectron spectroscopy (XPS) characterization was performed on a PHI-1600 ESCA spectrometer using Mg Kα (1253.6 eV) as radiation source. The analyzer chamber pressure was maintained at 5 × 10^{-8} Pa. The binding energies were calibrated using C 1s peak at 284.6 eV as standard and quoted with a precision of ±0.2 eV. The photoluminescence (PL) measurement was carried out on the Fluorolog3 photoluminescence spectrometer (Horiba Jobin Yvon, Japan) at room temperature using the excitation wavelength of 325 nm. Extended X-ray absorption fine structure (EXAFS) measurements were performed at the XAFS station in 14W1 beamline of Shanghai Synchrotron Radiation Facility (SSRF) operating at 250 mA and 3.5 GeV. The Ti K-edge absorption spectra of H-600 and N-600 were recorded in transmission mode at room temperature. The harmonic content in monochrome beam was reduced by using a Si(111) double crystal monochromator. In order to compensate for the diminishing amplitude, the back-
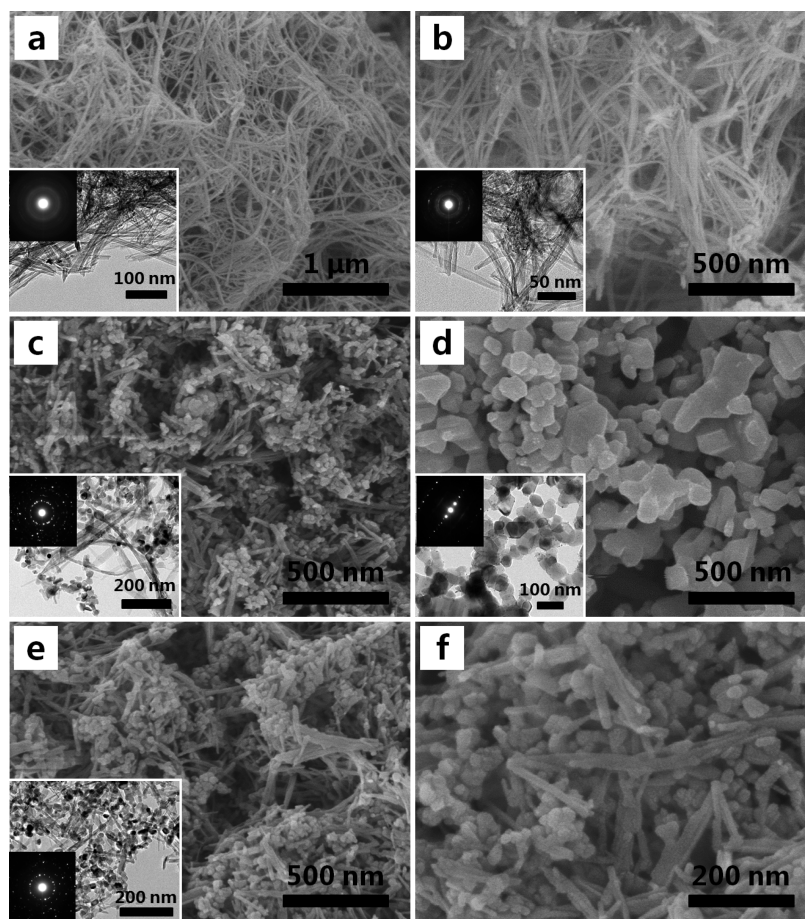
Figure 2. FESEM images illustrating the morphological evolution during thermal annealing in N₂ or H₂ at different temperature: (a) KTO nanowires, (b) N-400, (c) N-600, (d) N-800, (e) H-600, (f) H-600 image with higher magnification. The insets are the TEM images and the associated SEAD patterns corresponding to each sample.

subtracted EXAFS function was converted into k space and weighted by k^3. The Fourier transforming of k^3-weighted EXAFS data was performed in the range of $k = 3-12$ Å^{-1} using a Hanning window function.

2.4. Photocatalytic Hydrogen Production Measurement. The photocatalytic activity of the samples for water splitting was evaluated by monitoring the generated H₂. The measurement was carried out in the equipment of Labsolar-III AG system supplied by Beijing Perfectlight Technology Co., Ltd. In a typical procedure, 25 mg of photocatalyst was dispersed in 100 mL of an aqueous solution of methanol (1:1 by volume). The irradiation light source was a 300 W Xe lamp with an AM 1.5G filter. The generated H₂ was detected per 0.5 h by an online gas chromatography (GC) using a thermal conductivity detector (TCD).

3. RESULTS AND DISCUSSION

Figure 2a shows the FESEM image of the prepared titanate nanowires (KTO). It can be seen that the KTO possesses a typical diameter of ~40 nm and a length up to several micrometers. The morphology of KTO exhibits significant change during the thermal annealing at different temperatures in nitrogen atmosphere. As the annealing temperature increases from 400 to 600 °C, some of the nanowires (Figure 2b) transform to nanoparticles and adhere to the surface of nanowires tightly (Figure 2c); further increase of annealing temperature to 800 °C leads to the total transformation of

nanowires to nanoparticles with the diameter sharply increasing to ~150 nm (Figure 2d). This evolution process can be more clearly described by the XRD results and the selected area electron diffraction (SAED) patterns (insets in Figure 2). As shown in Figure 3, it is seen that the KTO exhibits a group of diffraction peaks attributable to K₂Ti₆O₁₃ phase (JCPDS No.
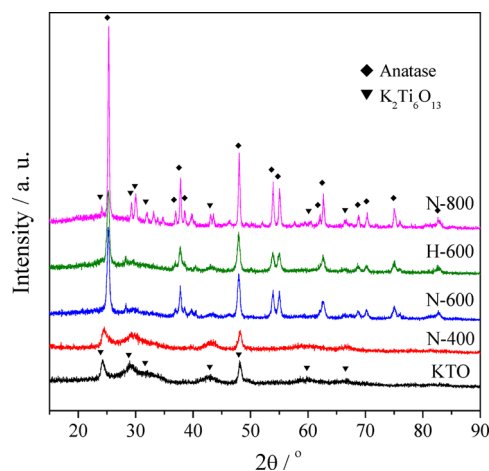

Figure 3. XRD patterns of KTO and the samples treated at different temperatures in nitrogen (N-400, N-600, and N-800) or hydrogen (H-600).
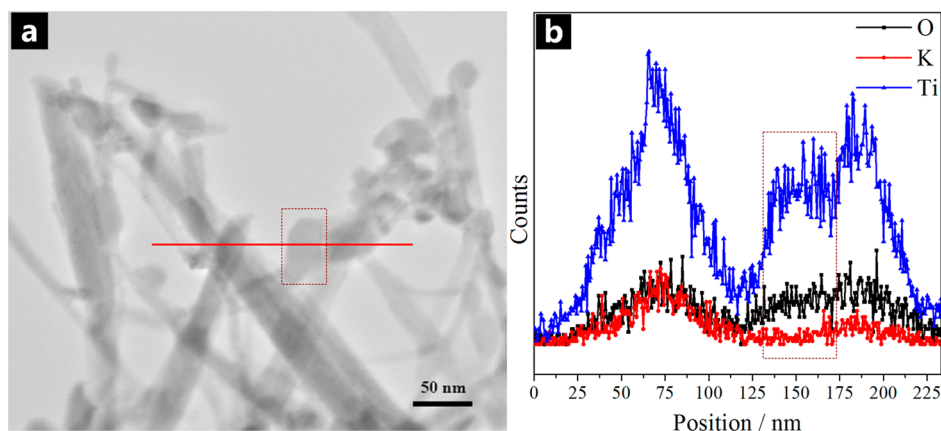
Figure 4. (a) STEM image of H-600. (b) The corresponding profile of EDS line-scanning along the red line marked in (a).
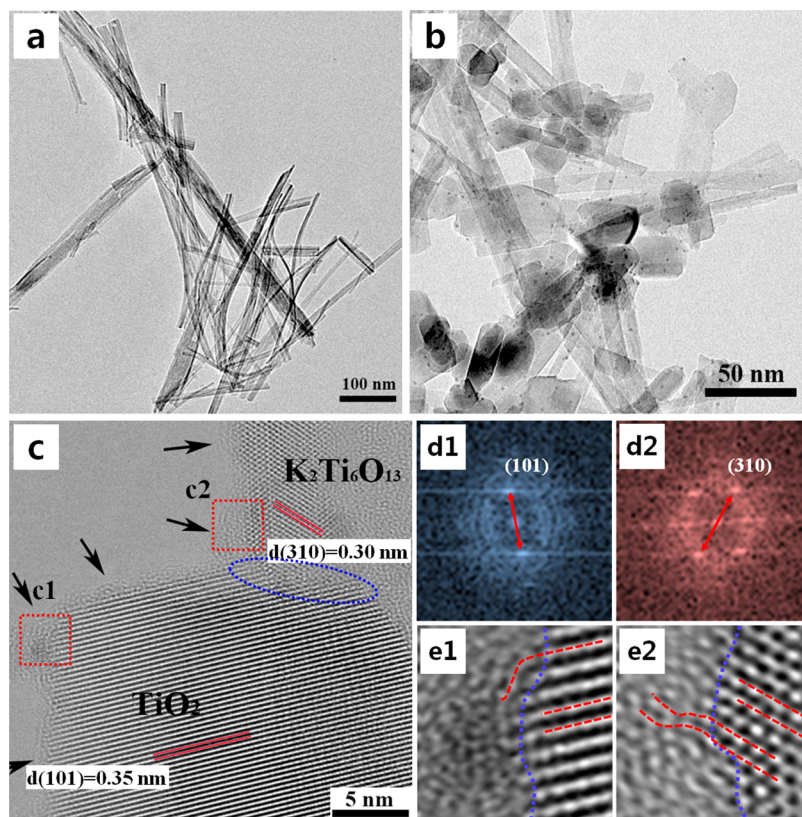

Figure 5. (a) TEM image of pristine KTO nanowires. (b) TEM image of H-600. (c) HRTEM image of H-600. (d1) and (d2) are the FFT images of the selected areas in (c) marked with c1 and c2. (e1) and (e2) are the IFFT images performed from (d1) and (d2) on the red arrow pointed spots.

40-0403). After thermal annealing at 400 °C in nitrogen, the crystal structure of $K_2Ti_6O_{13}$ is well retained, consistent with the results of morphology evolution (Figure 2b). When the annealing temperature rises to 600 °C, the diffraction peaks of anatase (JCPDS No. 21-1272) can be clearly observed, indicating that the in situ generation of anatase phase and a titanate−anatase heterostructure can be obtained by thermal annealing of titanate nanowires.

Inspired by this interesting finding, a hydrogenation method was used for the in situ synthesis the heterostructure and hydrogenated surface disorder. The hydrogenation temperature for Pt/KTO is optimized by H_2 temperature-programmed reduction (H_2-TPR) method, which is often used to characterize the reducible oxygen species.[20] Based on the H_2-TPR result

(Figure S1), it is thought that 600 °C is an appropriate temperature, at which the surface lattice oxygen species can be reduced without destroying the crystal structure. The samples treated at 600 °C in N_2 (N-600) or H_2 (H-600) display similar morphology (Figure 2e) and XRD patterns, suggesting the similarity of their bulk structure. From Figure 2e, it can still be seen that the nanoparticles tightly adhere to the surface of nanowires. Combined with the results of XRD and morphology, it is deduced that the titanate−anatase heterostructure should have been in situ-generated during the thermal annealing process.

The STEM image of H-600 is shown in Figure 4a, and the corresponding profile of EDS line-scanning along the red line marked in Figure 4a is shown in Figure 4b. Generally, the

strong peak indicates the high element concentration in the corresponding area.[32] From Figure 4b, it is observed that the peak intensities of O, K, and Ti elements increase simultaneously in the left region, demonstrating that the nanowires are titanate. However, in the dotted red box region, only the peaks of Ti and O elements with certain intensities can be observed, suggesting the formation of Ti oxide phases such as anatase phase. This deduction is supported by the appearance of the diffraction peaks of anatase in the XRD pattern of H-600 (Figure 3). The above STEM-EDS line-scanning results further demonstrate the in situ generation of titanate−anatase heterostructure in H-600 during the thermal annealing treatment.

Figure 5a,b show the morphology of pristine KTO nanowires and the hydrogenated H-600 with titanate−anatase hetero-structure. It is seen that the in situ-generated anatase nanoparticles are tightly coupled on the surface of KTO nanowires. The loaded Pt nanoparticles with a diameter of ∼2 nm are dispersed well on the surface of the heterostructure (Figure 5b and Figure S2). The HRTEM image of H-600 displayed in Figure 5c directly evidences that the energetically stable crystal facet of anatase TiO_2 (101) has grown in the conjunction with KTO nanowires. What's more, a disordered surface layer with ∼1 nm thickness coating on the crystalline core can also be observed. To further investigate this disordered shell, we performed the Fast Fourier Transform (FFT) in two selected areas marked with c1 and c2 in Figure 5c. The two FFT images taken from the dotted red boxes are obviously different, exhibiting the typical facets of anatase (101) and titanate (310), respectively. The Inverse Fast Fourier Transform (IFFT) was also performed on the red arrow pointed spots in Figure 5d1,d2.[20] Both the IFFT images show two different areas, namely, an ordered lattice area with periodic atomic arrangement and a significantly distorted lattice area, which are divided by the blue dash line. Along the red dashed lines, the distortion of crystal lattice can be clearly observed. In addition, the HRTEM image of N-600 displayed in Figure S3 shows no disordered shell on the surface of the formed heterostructure, demonstrating that the disordered shell cannot be formed under inert atmosphere. All the above results confirm that the in situ formation of heterostructure and surface disorderd shell has been simultaneously achieved by the facile hydrogenation treatment on the titanate nanowires.

The photocatalytic performance of the as-prepared catalysts for water splitting was evaluated under the simulated solar light irradiation. Figure 6a shows the time-dependent photocatalytic hydrogen evolution of the photocatalysts. It is found that the Pt/KTO exhibits the lowest hydrogen production rate of 10.8 $\mu mol·h^{-1}$, and the N-400 shows an average hydrogen production rate of 15.5 $\mu mol·h^{-1}$; such slight change may result from their similar structure as indicated by the XRD results and SEM images. The sample N-600 presents a remarkably improved hydrogen production rate of 158.2 $\mu mol·h^{-1}$, which is about 15 times to that of Pt/KTO nanowires. The excellent performance of N-600 could be ascribed to the formation of titanate−anatase heterostructure during thermal annealing at 600 °C. However, the sample N-800 displays lower photocatalytic activity as compared with that of N-600. The sharply increased nanoparticle size for both anatase and titanate can account for this significant activity reduction (Figure 2d), because the growth of the two individual phases would separate themselves from each other, weakening their interaction and decreasing the contact areas at the
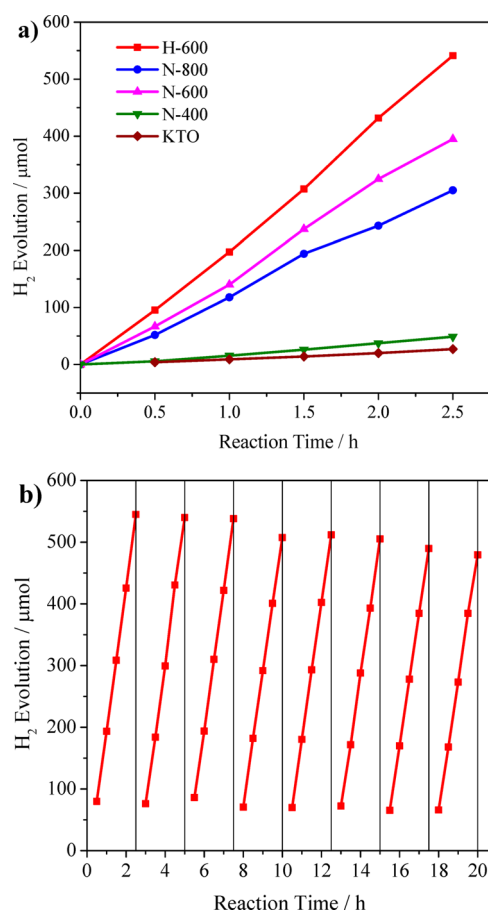

Figure 6. (a) Time-dependent H_2 production over different photocatalysts under simulated solar light irridiation. Photocatalyst (0.025 g) was dispersed in a 100 mL methanol solution (1:1 in volume). (b) Cyclic tests of H_2 production over H-600 under simulated solar light irradiation.

interface; as a result, the efficiency for the fast migration and separation of e^-−h^+ pairs is decreased. In addition, comparing the hydrogen production rates of the two samples annealed at the same temperature of 600 °C but in different atmospheres (N_2 or H_2), we find that the sample H-600 is much more active for water splitting, giving a hydrogen production rate of 216.5 $\mu mol·h^{-1}$. The further increased activity should result from the surface disordered shell formed in hydrogenation. The results of cyclic tests of H-600 are shown in Figure 6b, from which it is seen that this catalyst shows rather stable photocatalytic activity even after used for eight cycles. A very slight decrease of the activity may be caused by the gradual consumption of the sacrificial agent. These investigations demonstrate that the in situ simultaneous generation of titanate−anatase heterostruc-ture and surface disordered shell is a highly efficient strategy for the preparation of highly active and stable photocatalysts for water splitting.

Figure 7a shows the UV−vis diffuse reflectance spectra of the samples. It is seen that the as-synthesized KTO nanowires show a strong absorption in the UV region with the absorption edge appearing at ∼365 nm. After annealed in nitrogen atmosphere, all the samples show a slight red shift of the absorption edges, which could be ascribed to the presence of anatase (absorption edge located at ∼400 nm). When treated in hydrogen at 600 °C, the sample H-600 shows a very broad absorption, extending the light absorption to visible and near-infrared light region. To
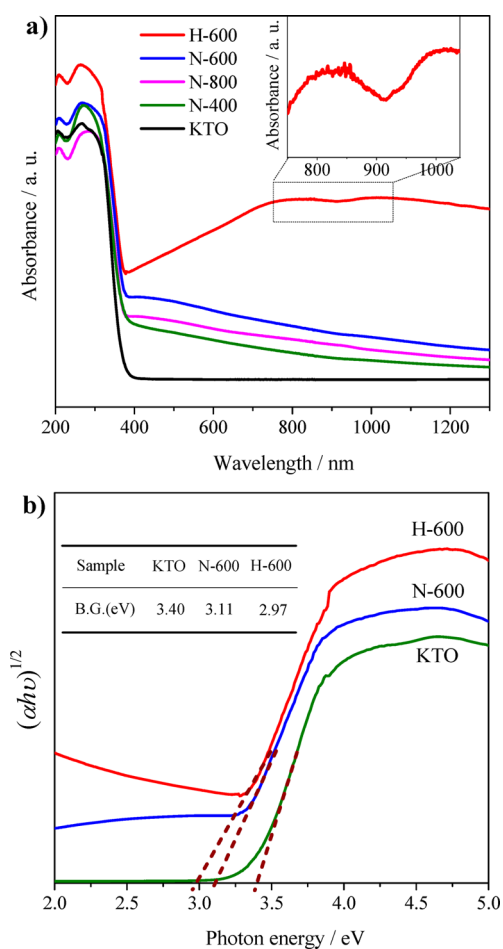
Figure 7. (a) UV−vis diffuse reflectance spectra of the as-prepared photocatalysts, the inset displays details in the 750 to 1050 nm wavelength region for H-600. (b) The corresponding Kubelka−Munk transformed diffuse reflectance spectra. The inserted table shows the band gap of the three typical samples obtained by extending the vertical segment to the $h\nu$ axis.

investigate the influence of such remarkably changed light absorption on photocatalytic activity, the hydrogen production rate of H-600 is also measured under only visible and infrared light by using a cutoff filter ($\lambda > 420$ nm). It is found that the rate of hydrogen production sharply dropped to a very low level which can hardly be detected; such an amount of hydrogen is negligible as compared with the hydrogen production under the simulated solar light. This result demonstrates that the increased absorption to visible and infrared light has little influence on the total hydrogen production rate; the high performance of H-600 should be resulted from the in situ-generated titanate−anatase heterostructure and the hydrogenated surface disordered shell.

The band gap energy (E_g) for the samples is estimated by using the Tauc eqn.[33,34]

$$\alpha h\nu = C_1 (h\nu - E_g)^2 \tag{1}$$

Where α is the optical absorption coefficient, C_1 is the absorption constant, and $h\nu$ is the photon energy. Figure 7b shows the plots of $(\alpha h\nu)^{1/2}$ versus $h\nu$ for KTO nanowires, N-600 and H-600. By extending the vertical segment to the $h\nu$ axis, the band gap (E_g) can be obtained.[31,35] The inserted table in Figure 7b reveals the band gap of the three typical samples.

The KTO nanowires exhibit a band gap as high as 3.40 eV, whereas the heterostructured samples N-600 and H-600 show decreased band gaps of 3.11 and 2.97 eV, respectively, which is consistent with the red shift of absorption edges for these two samples. The narrower band gap should be related to the presence of anatase in the two heterostructured samples. In particular, the inset in Figure 7a shows an abrupt change at approximately 910 nm (1.36 eV), indicating that the optical gap of H-600 is substantially narrower than other photocatalysts. Such narrowed band gap could be attributed to the generated surface disordered shell because it can result in some band tail states and diminish the band gap.[16]

The surface chemical bonding and element binding energy of the samples are characterized by XPS, the results of which are shown in Figure 8. It is found that the K 2p and Ti 2p XPS
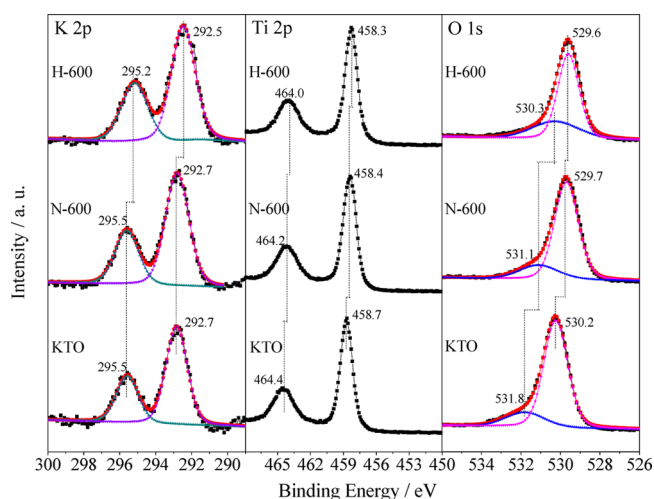

Figure 8. High-resolution XPS spectra of K 2p, Ti 2p, and O 1s of KTO, N-600, and H-600.

spectra for KTO, N-600 and H-600 are almost identical, indicating the similar bonding environments of K and Ti atoms before and after thermal annealing. The Ti $2p_{3/2}$ and $2p_{1/2}$ peaks centered at 458.5 and 464.3 eV could be assigned to Ti^{4+} ions in Ti^{4+}-O bonds.[36,37] The O 1s spectra of the three samples show obvious difference and they can be deconvoluted into two peaks by using the peak-fitting deconvolution. Compared with that of KTO, the lower O 1s binding energy position of N-600 could be ascribed to the in situ-generated anatase. The surface Ti−OH ratios of KTO and N-600 are very close to each other. However, for the hydrogenated sample H-600, both the surface lattice oxygen (O_L, 529.5 ± 0.2 eV) species and those surface Ti−OH groups (O_{OH}, 531.0 ± 0.2 eV)[38] shift to a lower binding energy positions with the ratio of O_{OH} increasing (Table S1). The ratio of $O_{OH}/(O_{OH}+O_L)$, correlating with the hydrophilicity of the catalyst surface, can affect the photoactivity.[38,39] In addition, the increased O_{OH} signal can also indirectly demonstrate the formation of defects, because the dissociated H· can react with lattice oxygen to form surface Ti−OH and V_o's.[20] To confirm this point, the extended X-ray absorption fine structure (EXAFS) was used to further investigate the hydrogenated samples. The obtained radial structure functions (RSFs) of Ti K-edge of H-600 and N-600 are presented in Figure 9. It is seen that the RSFs of these two samples show three coordination peaks around 1.5, 2.5, and 3.4 Å, which can be ascribed to the scattering of Ti−O (the first
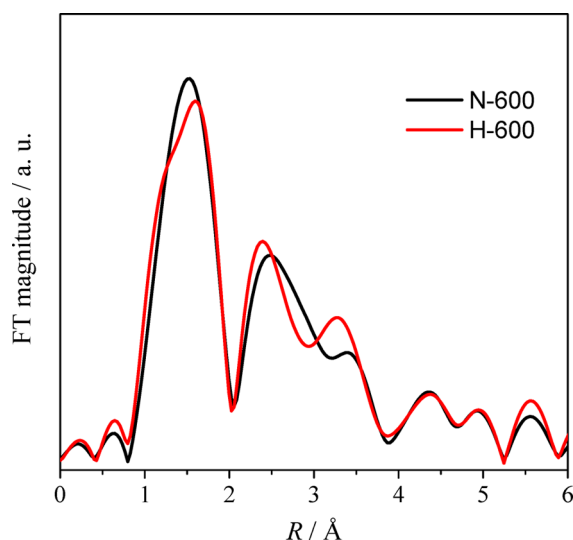
Figure 9. Radial structure functions (RSFs) of Ti K-edge of H-600 and N-600 obtained from the extended X-ray absorption fine structure (EXAFS) spectra.

Figure 10. Photoluminescence emission spectra of KTO, N-600, and H-600 using the excitation wavelength of 325 nm.

shell), Ti−Ti (the second shell), and a mixture of Ti−O, Ti−Ti, and Ti−K (the third shell), respectively.[40] It is noticed that the coordination peaks of the second and third shells of H-600 appear at lower R positions as compared with those of N-600, which implies a contraction of the interplanar distances induced by the presence of V_o's in the bulk structure of H-600.[19] In addition, by calculating and comparing the areas of the first coordination peaks (R = 1.1−2.0 Å) for H-600 and N-600, which corresponds to Ti−O shell and correlates with the Debye−Waller factor, it is found that the sample H-600 shows a slightly reduced peak area, which suggests that after hydrogenation less oxygen atoms are coordinated with each central Ti atom in H-600. So, it is deduced that the hydrogenation may have removed some bulk oxygen, forming bulk oxygen vacancies which cannot be characterized by the surface technique of XPS. During hydrogenation, the surface lattice oxygen should be removed first, forming surface V_o's, but at high temperature, the bulk lattice oxygen possesses high mobility, which may diffuse from bulk to surface; as a result, no V_o's in the surface disordered shell are detected. The change of interplanar distances as reflected in the RSFs is an important evidence to prove the existence of V_o's in the bulk structure of the catalyst H-600. The presence of V_o's can increase the donor density and serve as electron donors,[15] and the increased electron density can make the Fermi level of the catalyst shift toward the conduction band. Such upshift of Fermi level can improve the charge migration and separation at the heterostructure interface, leading to the band bending. Thus, the charge transport as well as the electron transfer between the titanate−anatase heterostructure is enhanced, and thus, the superior photocatalytic performance of H-600 is achieved.

The photoluminescence (PL) emission spectra are often used to evaluate the transfer and separation of charge carriers because PL emission results from the recombination of free carriers.[41] The ambient PL spectra of KTO, N-600, and H-600 in the wavelength range of 350−700 nm are shown in Figure 10. It is obvious that the as-synthesized KTO nanowires display a very broad and very strong emission spectrum in the wavelength range of 350−700 nm, whereas those of N-600 and H-600 are much narrower and lower. The remarkably
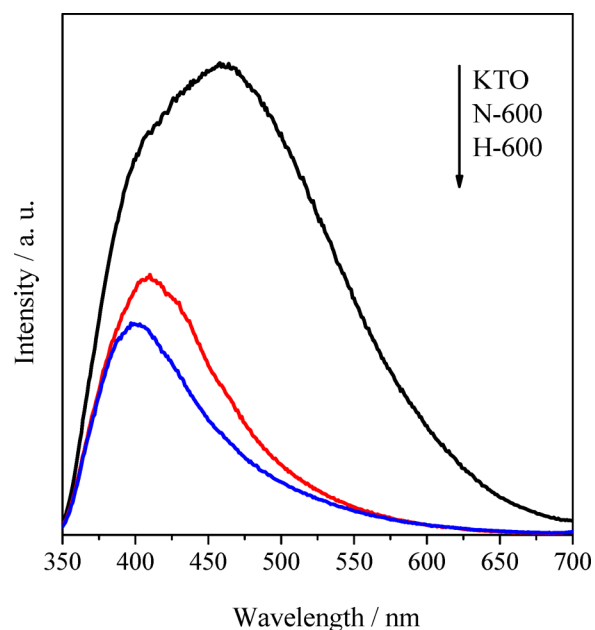
decreased emission can be assigned to the in situ-generated titanate−anatase heterojunction at the interface of the two semiconductors. The instinctive different band edge positions of anatase and titanate facilitate the separation and transfer of the charge carriers, resulting in less recombination.[35] The lower photoluminescence emission intensity of H-600 than N-600 should be caused by the distortion of lattice structure such as the generation of bulk V_o's and the formation of surface disordered shell, which may have prevented the rapid recombination of photoexcited charge carriers.[15]

The valence bands of KTO nanowires and H-600 were characterized by valence band XPS (Figure 11a). The edge of the maximal energy of KTO nanowires is at about 2.28 eV below the Fermi energy, which is estimated by linear extrapolation of the peak to the baseline. Because the band gap of KTO is 3.40 eV (UV−vis results), the conduction band minimum should occur at about −1.12 eV.[16,19] After in situ hydrogenation, the valence band of H-600 exhibits an obvious difference. The valence band absorption onset shows a blue-shift to 1.08 eV, and the maximal energy associated with the band tail further blue-shifts toward the vacuum level at −0.53 eV. Combined with the results of UV−vis absorption, an energy band diagram is proposed in Figure 11b to illustrate the respective band position of KTO and H-600, similar to that in the reported work.[19] The band tail states of valence band of H-600 are induced by the distortion of crystal lattice of titanate and anatase. The lattice disorder would produce a lot of midgap states; large amounts of midgap states can form a continuum, which extends to valence band and overlaps with them; as a result, the band tail states are generated.[16] The V_o's localized states generated by hydrogenation are also taken into account to this scheme, which are below the conduction band minimum about 0.7−1.0 eV.[19] The optical transitions between band tail, V_o's localized states and conduction band would induce charge transfer from the O 2p orbital to the Ti 3d orbital,[16] giving the visible and near-infrared light absorption; the localization of the as-generated elections and holes can inhibit the recombination of charge carriers. In a word, the valence band XPS confirms
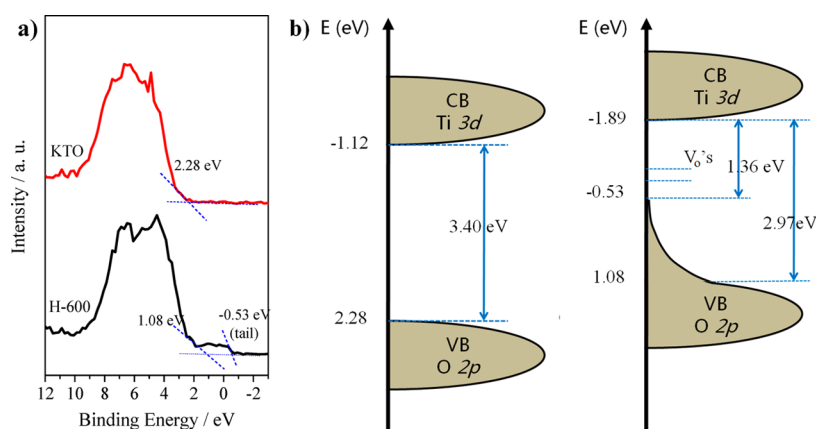
Figure 11. (a) Valence band XPS spectra of KTO and H-600. (b) Proposed energy band diagram of KTO (left) and H-600 (right).

that the as-formed heterostructure and surface disordered shell do have a big impact on the valence band structure, leading to the unusual photocatalytic performance.

4. CONCLUSIONS

In conclusion, by an in situ hydrogenation on KTO nanowires, we successfully synthesized a heterostructured titanate–anatase catalyst with a disordered surface shell, exhibiting a hydrogen production rate of 216.5 μmol·h^{-1} for water splitting, which is about 20 times higher than the untreated Pt-loaded KTO nanowires without heterostructure and surface disordered shell. The superior catalytic performance of this catalyst can be attributed to the synergistic effect of the in situ-generated heterostructure and the hydrogenation-induced surface disordered shell, which can not only promote the migration of electron–hole pairs but also inhibit the recombination of the generated charge carriers. The catalyst design and preparation strategy in this work is valuable and could be referenced in the design of other composite photocatalytic systems.

■ ASSOCIATED CONTENT

Ⓢ Supporting Information

The following file is available free of charge on the ACS Publications website at DOI: 10.1021/acscatal.5b00055.

H$_2$-TPR profile of Pt-loaded titanate nanowires, higher magnification TEM image of H-600 and size distribution of Pt nanoparticles, HRTEM image of N-600, ratios of different surface oxygen species (PDF)

■ AUTHOR INFORMATION

Corresponding Authors
*E-mail: mengm@tju.edu.cn. Tel./Fax: +86 22-2789-2275.
*E-mail: zphu@nankai.edu.cn.

Notes

The authors declare no competing financial interest.

■ ACKNOWLEDGMENTS

■ REFERENCES

(1) Chen, X.; Shen, S.; Guo, L.; Mao, S. S. *Chem. Rev.* **2010**, *110*, 6503−6570.
(2) Kudo, A.; Miseki, Y. *Chem. Soc. Rev.* **2009**, *38*, 253−278.
(3) Kubacka, A.; Fernandez-Garcia, M.; Colon, G. *Chem. Rev.* **2012**, *112*, 1555−1614.
(4) Maeda, K.; Domen, K. *J. Phys. Chem. Lett.* **2010**, *1*, 2655−2661.
(5) Maeda, K. *ACS Catal.* **2013**, *3*, 1486−1503.
(6) Tang, J.; Durrant, J. R.; Klug, D. R. *J. Am. Chem. Soc.* **2008**, *130*, 13885−13891.
(7) Serpone, N.; Lawless, D.; Khairutdinov, R.; Pelizzetti, E. *J. Phys. Chem.* **1995**, *99*, 16655−16661.
(8) Nagaveni, K.; Hegde, M. S.; Madras, G. *J. Phys. Chem. B* **2004**, *108*, 20204−20212.
(9) Lin, T.; Yang, C.; Wang, Z.; Yin, H.; Lu, X.; Huang, F.; Lin, J.; Xie, X.; Jiang, M. *Energy Environ. Sci.* **2014**, *7*, 967−972.
(10) Chen, X.; Burda, C. *J. Am. Chem. Soc.* **2008**, *130*, 5018−5019.
(11) Yang, C.; Wang, Z.; Lin, T.; Yin, H.; Lv, X.; Wan, D.; Xu, T.; Zheng, C.; Lin, J.; Huang, F.; Xie, X.; Jiang, M. *J. Am. Chem. Soc.* **2013**, *135*, 17831−17838.
(12) Liu, B.; Liu, L.; Lang, X.; Wang, H.; Lou, X.; Aydil, E. S. *Energy Environ. Sci.* **2014**, *7*, 2592−2597.
(13) Myung, S. T.; Kikuchi, M.; Yoon, C. S.; Yashiro, H.; Kim, S. J.; Sun, Y. K.; Scrosati, B. *Energy Environ. Sci.* **2013**, *6*, 2609−2614.
(14) Liu, N.; Schneider, C.; Freitag, D.; Hartmann, M.; Venkatesan, U.; Müller, J.; Spiecker, E.; Schmuki, P. *Nano Lett.* **2014**, *14*, 3309−3313.
(15) Wang, G.; Wang, H.; Ling, Y.; Tang, Y.; Yang, X.; Fitzmorris, R. C.; Wang, C.; Zhang, J. Z.; Li, Y. *Nano Lett.* **2011**, *11*, 3026−3033.
(16) Chen, X.; Liu, L.; Yu, P. Y.; Mao, S. S. *Science* **2011**, *331*, 746−750.
(17) Wang, Z.; Yang, C.; Lin, T.; Yin, H.; Chen, P.; Wan, D.; Xu, F.; Huang, F.; Lin, J.; Xie, X.; Jiang, M. *Adv. Funct. Mater.* **2013**, *23*, 5444−5450.
(18) Zheng, Z.; Huang, B.; Lu, J.; Wang, Z.; Qin, X.; Zhang, X.; Dai, Y.; Whangbo, M. H. *Chem. Commun.* **2012**, *48*, 5733−5735.
(19) Naldoni, A.; Allieta, M.; Santangelo, S.; Marelli, M.; Fabbri, F.; Cappelli, S.; Bianchi, C. L.; Psaro, R.; Dal Santo, V. *J. Am. Chem. Soc.* **2012**, *134*, 7600−7603.
(20) Zhu, Y.; Liu, D.; Meng, M. *Chem. Commun.* **2014**, *50*, 6049−6051.
(21) Wang, Z.; Yang, C.; Lin, T.; Yin, H.; Chen, P.; Wan, D.; Xu, F.; Huang, F.; Lin, J.; Xie, X.; Jiang, M. *Energy Environ. Sci.* **2013**, *6*, 3007−3014.
(22) Yu, X.; Kim, B.; Kim, Y. K. *ACS Catal.* **2013**, *3*, 2479−2486.
(23) Wang, X.; Xu, Q.; Li, M.; Shen, S.; Wang, X.; Wang, Y.; Feng, Z.; Shi, J.; Han, H.; Li, C. *Angew. Chem., Int. Ed.* **2012**, *51*, 13089−13092.
(24) Cao, T.; Li, Y.; Wang, C.; Shao, C.; Liu, Y. *Langmuir* **2011**, *27*, 2946−2952.

(25) Wang, H.; Zhang, L.; Chen, Z.; Hu, J.; Li, S.; Wang, Z.; Liu, J.; Wang, X. *Chem. Soc. Rev.* **2014**, *43*, 5234−5244.

(26) Lee, Y. S.; Heo, J.; Siah, S. C.; Mailoa, J. P.; Brandt, R. E.; Kim, S. B.; Gordon, R. G.; Buonassisi, T. *Energy Environ. Sci.* **2013**, *6*, 2112−2118.

(27) Lingampalli, S. R.; Gautam, U. K.; Rao, C. N. R. *Energy Environ. Sci.* **2013**, *6*, 3589−3594.

(28) Boppana, V. B. R.; Lobo, R. F. *ACS Catal.* **2011**, *1*, 923−928.

(29) Wang, X.; Li, Z.; Shi, J.; Yu, Y. *Chem. Rev.* **2014**, *114*, 9346−9384.

(30) Zhu, H. Y.; Lan, Y.; Gao, X. P.; Ringer, S. P.; Zheng, Z. F.; Song, D. Y.; Zhao, J. C. *J. Am. Chem. Soc.* **2005**, *127*, 6730−6736.

(31) Xiong, Z.; Zhao, X. S. *J. Am. Chem. Soc.* **2012**, *134*, 5754−5757.

(32) Li, G.; Wang, F.; Jiang, Q.; Gao, X.; Shen, P. *Angew. Chem., Int. Ed.* **2010**, *49*, 3653−3656.

(33) Huxter, V. M.; Mirkovic, T.; Nair, P. S.; Scholes, G. D. *Adv. Mater.* **2008**, *20*, 2439−2443.

(34) Zhou, W.; Du, G.; Hu, P.; Li, G.; Wang, D.; Liu, H.; Wang, J.; Boughton, R. I.; Liu, D.; Jiang, H. *J. Mater. Chem.* **2011**, *21*, 7937−7945.

(35) Ng, J.; Xu, S.; Zhang, X.; Yang, H. Y.; Sun, D. D. *Adv. Funct. Mater.* **2010**, *20*, 4287−4294.

(36) Cui, H.; Zhao, W.; Yang, C.; Yin, H.; Lin, T.; Shan, Y.; Xie, Y.; Gu, H.; Huang, F. *J. Mater. Chem. A* **2014**, *2*, 8612−8616.

(37) Ardizzone, S.; Bianchi, C. L.; Cappelletti, G.; Naldoni, A.; Pirola, C. *Environ. Sci. Technol.* **2008**, *42*, 6671−6676.

(38) Naldoni, A.; Bianchi, C. L.; Pirola, C.; Suslick, K. S. *Ultrason. Sonochem.* **2013**, *20*, 445−451.

(39) Ardizzone, S.; Bianchi, C. L.; Cappelletti, G.; Gialanella, S.; Pirola, C.; Ragaini, V. *J. Phys. Chem. B* **2007**, *111*, 13222−13231.

(40) Zhou, W.; Li, W.; Wang, J.; Qu, Y.; Yang, Y.; Xie, Y.; Zhang, K.; Wang, L.; Fu, H.; Zhao, D. *J. Am. Chem. Soc.* **2014**, *136*, 9280−9283.

(41) Zhang, W. F.; Zhang, M. S.; Yin, Z.; Chen, Q. *Appl. Phys. B: Laser Opt.* **2000**, *70*, 261−265.